

A TECHNIQUE OF REMOVING LARGE-SCALE VARIATIONS IN ASTRONOMICAL OBSERVATIONS

JUNGYEON CHO

Department of Astronomy and Space Science, Chungnam National University, Daejeon, Korea; jcho@cnu.ac.kr
Draft version November 10, 2021

ABSTRACT

In many astrophysical systems, smoothly-varying large-scale variations coexist with small-scale fluctuations. For example, a large-scale velocity or density gradient can exist in molecular clouds that exhibit small-scale turbulence. In redshifted 21cm observations, we also have two types of signals - the Galactic foreground emissions that change smoothly and the redshifted 21cm signals that change fast in frequency space. Sometimes the large-scale variations make it difficult to extract information on small-scale fluctuations. We propose a simple technique to remove smoothly varying large-scale variations. Our technique relies on multi-point structure functions and can obtain the magnitudes of small-scale fluctuations. It can also help us to filter out large-scale variations and retrieve small-scale maps. We discuss applications of our technique to astrophysical observations.

Keywords: methods: data analysis — ISM: general — cosmology: observations — turbulence

1. INTRODUCTION

In many astrophysical fluids, smooth large-scale variations are overlaid with fast-varying small-scale fluctuations. For example, magnetic fields in molecular clouds may consist of smoothly-varying mean components and shorter-scale turbulence components (see, for example, Girart et al. 2006; Hildebrand et al. 2009; Houde et al. 2009). Velocity fields in molecular clouds also exhibit large-scale gradients, as well as small-scale turbulent fluctuations (Imara & Blitz 2011). The separation of signals into large-scale and small-scale ones is not limited to spatial fluctuations. In observations of the redshifted 21 cm lines, we may separate smoothly varying large-scale foreground components and fast-fluctuating small-scale cosmological components in frequency space (Morales et al. 2006; Cho et al. 2012). We may also separate time-series data into two components.

If large-scale variations and small-scale fluctuations coexist, the large-scale components sometimes make it difficult to obtain information on small-scale fluctuations. For many applications, it is necessary to accurately measure small-scale fluctuations. For example, we could constrain turbulence parameters by observing the standard deviation, skewness, or kurtosis of column density (e.g., Burkhart et al. 2009). If there is no large-scale variations of column density, it may be straightforward to obtain those quantities from observations. However, when there are large-scale variations, they will certainly affect all those quantities.

The situation is similar for centroid velocity (for an optically thin line), which is equal to the intensity-weighted average velocity (see Section 2.2 for mathematical definition). Centroid velocity contains information on turbulence velocity field and therefore has been used to diagnose properties of interstellar turbulence (von Hoerner 1951; Dickman & Kleiner 1985; Kleiner & Dickman 1985; O'Dell & Castañeda 1987; Miesch & Bally 1994; Esquivel et al. 2007). Therefore accurate measurements of the small-scale centroid velocity fluctuations is important for the study of interstellar turbulence.

Centroid velocity is also important for measurement of

interstellar magnetic fields (Cho & Yoo 2016; González-Casanova & Lazarian 2017). The Chandrasekhar-Fermi method (Chandrasekhar & Fermi 1953) is a popular and simple technique to obtain strengths of interstellar magnetic fields projected on the plane of the sky, which makes use of polarized emission in FIR/sub-mm wavelengths from magnetically aligned grains (Gonatas et al. 1990; Lai et al. 2001; Di Francesco et al. 2001; Crutcher et al. 2004; Girart et al. 2006; Curran & Chrysostomou 2007; Heyer et al. 2008; Mao et al. 2008; Tang et al. 2009; Sugitani et al. 2011; Pattle et al. 2017). The Chandrasekhar-Fermi method is based on the following assumption: If the mean magnetic field is strong, wandering of magnetic field lines is small and, therefore, variation of polarization angle is small¹. Cho & Yoo (2016) showed that, if there are N independent eddies along the line of sight (LOS), the variation of polarization angle ($\delta\phi$) is reduced by $\sim\sqrt{N}$ due to random averaging effect. If we use the Chandrasekhar-Fermi method, the reduction in $\delta\phi$ results in overestimation of magnetic field strength by a factor of \sqrt{N} . Cho & Yoo (2016) suggested that the standard deviation of centroid velocity divided by average line width can tell us about \sqrt{N} (see Cho (2017) for a heuristic explanation for this). Therefore accurate measurements of the small-scale centroid velocity fluctuations is important for the application of the Chandrasekhar-Fermi method. Since large-scale variations in the LOS velocity can severely affect the standard deviation of centroid velocity, it is necessary to remove the large-scale LOS velocity variations.

Fitting is frequently used to remove large-scale variations. For example, magnetic fields in molecular cores frequently show an hour-glass morphology (Schleuning 1998; Houde et al. 2004). As explained in the previous paragraph, the Chandrasekhar-Fermi method requires measurement of $\delta\phi$. However the large-scale magnetic

¹ In fact, the method assumes $\tan\delta\phi\sim\delta b/B_0(\approx M_A)$, where $\delta\phi$ is the variation of polarization angle, δb is the strength of fluctuating magnetic field, B_0 is the strength of the mean magnetic field projected on the plane of the sky, and M_A is the Alfvén Mach number.

morphology impedes accurate measurement of the quantity, which makes it difficult to apply the Chandrasekhar-Fermi method. To model the hour-glass shape large-scale magnetic fields, a fitting function of the form $x = g + gCy^2$, where g and C are constants, has been successfully used (Girart et al. 2006; Sugitani et al. 2010). However, in many cases, fitting requires knowledge on the large-scale variations *a priori*.

In this paper, we propose a technique to remove large-scale variations. Our main goal is to obtain the standard deviations of small-scale quantities. Nevertheless, our technique can be also used to filter out large-scale variations and retrieve small-scale maps. Our technique requires multi-point structure functions and does not rely on fitting method. We first describe theoretical backgrounds of our technique and numerical methods for testing our technique in Section 2. We present our results in Section 3. We give discussions and summary in Sections 4.

2. THEORETICAL CONSIDERATIONS AND NUMERICAL METHODS

2.1. Removal of large-scale variation with multi-point structure functions

Suppose that a quantity Q in real space exhibits a large-scale variation, as well as small-scale fluctuations (see Figure 1):

$$Q(\mathbf{x}) = Q_L(\mathbf{x}) + Q_S(\mathbf{x}). \quad (1)$$

We assume the spatial average $\langle Q_S(\mathbf{x}) \rangle$ is zero when we calculate the average on scales larger than the small-scale correlation length l_S :

$$\langle Q_S(\mathbf{x}) \rangle = 0 \quad (\text{if scale} > l_S). \quad (2)$$

Our goal is to remove the large-scale variation $Q_L(\mathbf{x})$ and obtain the standard deviation of the small-scale fluctuation σ_Q . In this subsection, we show that multi-point structure functions, rather than the conventional 2-point structure function, can effectively remove the large-scale variation.

2.1.1. Two-point structure function

In many problems, the usual 2-point second-order structure function for a variable Q ,

$$\text{SF}_2^{2pt}(r) = \langle |Q(\mathbf{x} + \mathbf{r}) - Q(\mathbf{x})|^2 \rangle_{\text{avg. over } \mathbf{x}}, \quad (3)$$

is frequently used to diagnose structures on different scales. In fact, it is related to power spectrum². However, we should be careful when we use SF_2^{2pt} . In the presence of a large-scale variation, it may fail to reveal small-scale structures correctly. If we select two points, \mathbf{x} and $\mathbf{x} + \mathbf{r}$, as in Figure 1(a), the difference of the large-scale quantity ($|\Delta_L^{2pt}| \equiv |Q_L(\mathbf{x}) - Q_L(\mathbf{x} + \mathbf{r})|$) can be larger than that of the small-scale quantity ($|\Delta_S^{2pt}| \equiv$

² If the one-dimensional power spectrum is proportional to k^{-m} (i.e., $E(k) \propto k^{-m}$), where k is the wavenumber, the 2-point second-order structure function becomes $\text{SF}_2^{2pt}(r) \propto r^{m-1}$ (see, for example, Monin & Iaglom 1975). In the case of a steep spectrum (i.e., $m > 3$), the 3-point structure function (see Equation (7)) should be used to reveal the correct spectral slope (Falcon et al. 2007; Lazarian & Pogosyan 2008; Cho & Lazarian 2009).

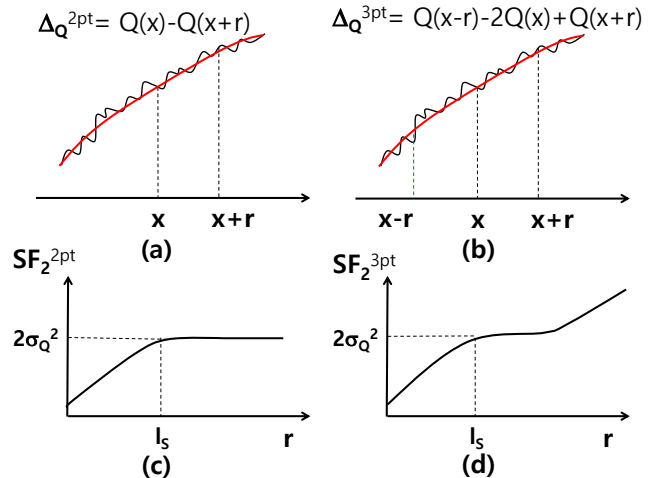


Figure 1. Large-scale variation and the 2-point and the 3-point structure functions. (a) The large-scale variation dominates the quantity Δ_Q^{2pt} if the separation r is large enough. (b) It is possible that the small-scale fluctuations can dominate the quantity Δ_Q^{3pt} even if r is large. (c) The behavior of a second-order structure function in the absence of a large-scale variation. (d) The behavior of a multi-point second-order structure function in the presence of large-scale variations. If the structure function successfully removes the large-scale effect, we will have an extended flat part ('plateau') on scales larger than l_S .

$|Q_S(\mathbf{x}) - Q_S(\mathbf{x} + \mathbf{r})|$), which results in

$$\text{SF}_2^{2pt} = \langle (\Delta_L^{2pt} + \Delta_S^{2pt})^2 \rangle \approx \langle (\Delta_L^{2pt})^2 \rangle \propto r^2 \quad (\text{if } |\Delta_L^{2pt}| > |\Delta_S^{2pt}|), \quad (4)$$

where $r \equiv |\mathbf{r}|$ and we assume that Δ_L^{2pt} varies smoothly. Therefore, if the large-scale variation dominates the small-scale fluctuations, it is not possible to reveal statistics of the small-scale fluctuations from SF_2^{2pt} .

2.1.2. Multi-point structure functions

If we use multi-point structure functions, we can remove substantial amount of the large-scale effects. Let us consider difference of Q constructed with 3-points:

$$\Delta_Q^{3pt} = Q(\mathbf{x} - \mathbf{r}) - 2Q(\mathbf{x}) + Q(\mathbf{x} + \mathbf{r}) \quad (5)$$

(see Figure 1(b)). It is trivial to show that Δ_Q^{3pt} can exactly eliminate a large-scale variation that has a constant slope. If the large-scale variation is so smooth that

$$|\Delta_L^{3pt}| < |\Delta_S^{3pt}|, \quad (6)$$

as in Figure 1(b), then the 3-point structure function

$$\text{SF}_2^{3pt} \equiv \frac{1}{3} \langle |Q(\mathbf{x} - \mathbf{r}) - 2Q(\mathbf{x}) + Q(\mathbf{x} + \mathbf{r})|^2 \rangle, \quad (7)$$

can capture small-scale fluctuations correctly.

We can also construct 4-point and 5-point second-order structure functions as follows:

$$\text{SF}_2^{4pt} \equiv \frac{1}{10} \langle |Q(\mathbf{x} - \mathbf{r}) - 3Q(\mathbf{x}) + 3Q(\mathbf{x} + \mathbf{r}) - Q(\mathbf{x} + 2\mathbf{r})|^2 \rangle, \quad (8)$$

$$\text{SF}_2^{5pt} \equiv \frac{1}{35} \langle |Q(\mathbf{x} - 2\mathbf{r}) - 4Q(\mathbf{x} - \mathbf{r}) + 6Q(\mathbf{x}) - 4Q(\mathbf{x} + \mathbf{r}) + Q(\mathbf{x} + 2\mathbf{r})|^2 \rangle \quad (9)$$

(see Section 4.4 for general definition). It is worth noting that SF_2^{4pt} and SF_2^{5pt} can exactly remove large-scale variations that follow a quadratic and a cubic polynomial, respectively.

2.1.3. The behavior of structure functions

Our primary goal is to obtain the standard deviation σ_Q of small-scale fluctuations. We may obtain σ_Q^2 from the shape of a second-order structure function. Let us consider small-scale turbulence with correlation length l_S . If there is *no* large-scale variation, the behavior of a second-order structure function may look like Figure 1(c). When the separation r is small (i.e., when $r < l_S$), the structure function reflects small-scale turbulence statistics and thus is an increasing function of r (see, Footnote 2). When $r > l_S$, $Q_S(\mathbf{x} + \mathbf{r})$ and $Q_S(\mathbf{x})$ are uncorrelated and the second-order structure function gives

$$\text{SF}_2 \approx 2\sigma_Q^2 \quad (\text{if } r > l_S). \quad (10)$$

In fact, all the second-order structure functions mentioned above will give this value when $r > l_S$.

On the other hand, if there is a large-scale variation and a multi-point structure function successfully removes a substantial part of it, then the behavior of the structure function will look like Figure 1(d)³. When $r < l_S$, the structure function is an increasing function of r . When $r > l_S$ the structure function becomes flat, because the large-scale variation is substantially removed. The value of the second-order structure function for the flat part is $\sim 2\sigma_Q^2$. As r increases further, the accuracy of removing the large-scale variation by the structure function gets worse and ultimately the large-scale variation makes the structure function increase again. If the large-scale variation is poorly removed, the flat part will be very short. The bottom line is that resolving the flat part (hereinafter ‘plateau’) is essential for obtaining σ_Q^2 .

2.2. Numerical methods

In the previous subsection, we argued that it is more advantageous to use multi-point SF_2 's to remove large-scale variations. In this paper, we test this idea using numerical calculations. The observable quantities we consider are the column density (Σ) and the velocity centroid (V_c). The column density and the velocity centroid are defined by

$$\Sigma = \int \rho \, dz, \quad (11)$$

$$V_c = \int \rho v_z \, dz \bigg/ \int \rho \, dz, \quad (12)$$

where z is along the LOS, ρ is the 3-dimensional (3D) density, and v_z is the LOS velocity. We consider two types of calculations.

³ Note that, if the large-scale gradient is *very small*, even the 2-point structure function can also show a similar behavior.

2.2.1. Simple sinusoidal large-scale variations

We generate data that contain both small-scale fluctuations and a large-scale variation from the following procedure. We take turbulence data as small-scale fluctuations⁴.

First, we generate 3D turbulence data from a direct numerical simulation of isothermal supersonic magnetohydrodynamic (MHD) turbulence, which contain only small-scale fluctuations. The computational domain is a cubic box of size 2π ($\equiv L$) and consists of 512^3 grid points. The simulation is identical to the model ‘KF20’ in Cho & Yoo (2016). The driving scale is about 20 times smaller than the size of the computational domain, which means that the typical size of largest energy-containing eddies is about 20 times smaller than the size of the computational box. The sonic and the Alfvénic Mach numbers are ~ 7 and ~ 0.7 , respectively. The fluid velocity is zero ($v = 0$), density is one ($\rho_0 = 1$), and the Alfvén speed of mean field is one ($B_0/\sqrt{4\pi\rho_0} = 1$) at $t=0$. Further description of the code can be found in Cho & Yoo (2016).

Our goal is to obtain the magnitudes of small-scale fluctuations of column density and velocity centroid. Since these fluctuations are related to 3D density and velocity (see Equations (11) and (12)), we plot time evolution of v^2 and $(\delta\rho)^2$ in the left panel of Figure 2, where v is the 3D velocity and $\delta\rho$ ($\equiv \rho - \rho_0$) is the fluctuating 3D density. The data we use are taken at $t \sim 6$, at which the r.m.s. velocity is ~ 0.7 and $\delta\rho \sim 1.6$. The right panel of Figure 2 shows spectra of the 3D velocity ($E_v(k)$) and density ($E_\rho(k)$). They have peaks at $k \sim 20$, which corresponds to the average driving wavenumber.

Second, using the data, we calculate column density (Equation (11)) and centroid velocity (Equation (12)). The LOS is along the z -direction and is perpendicular to the mean magnetic field. The standard deviations of column density and centroid velocity (*without* a large-scale variation) along the LOS are

$$\sigma_\Sigma \approx 90, \quad \text{and} \quad \sigma_{V_c} \approx 0.084, \quad (13)$$

and, therefore, we have

$$2(\sigma_\Sigma)^2 \approx 1.6 \times 10^4, \quad \text{and} \quad 2(\sigma_{V_c})^2 \approx 0.014 \quad (14)$$

(see Table 1).

Third, after calculating column density and centroid velocity, we add simple large-scale variations. The large-scale variations have the sinusoidal form

$$Q(\mathbf{x}) = A_Q \sin[k(x - \pi)], \quad k=1/2, 5/2, 9/2, \quad (15)$$

where $0 < x \leq 2\pi$ and Q is either column density or centroid velocity. The corresponding wavelengths of the large-scale variations are λ ($= 2\pi/k$) = $2L$, $2L/5$, and $2L/9$, respectively. The amplitude A is 1024 for column density (i.e., $A_\Sigma=1024$) and 1.0 for centroid velocity (i.e., $A_{V_c}=1.0$), which are ~ 10 times larger than the amplitudes of the corresponding small-scale fluctuations. We list properties of the turbulence data, including standard deviations of small-scale fluctuations (σ_Σ and σ_{V_c}), in Table 1 (see Model KF20).

⁴ Note that the small-scale data are not necessarily turbulence data. We use existing small-scale turbulence data for simplicity.

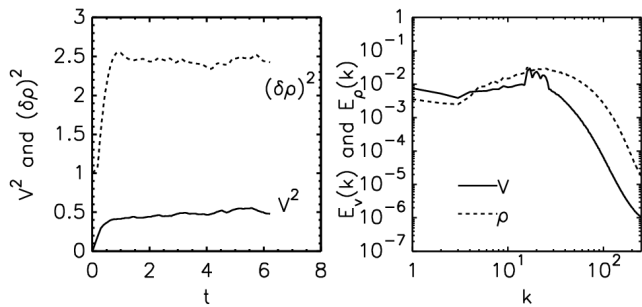


Figure 2. The Run K20. We drive a fluid at $k \sim 20$ and generate supersonic isothermal turbulence. We take data cubes from the run as small-scale fluctuating quantities. (a) Time evolution of 3-dimensional (3D) v^2 and $(\delta\rho)^2$. (b) The spectra of the 3D velocity (v) and density (ρ) at $t \sim 6$.

2.2.2. More complicated turbulent large-scale variations

In the previous subsection, we considered idealistic large-scale variations. To see if our technique works also for more complicated large-scale fluctuations, we take large-scale turbulence data as the large-scale variations. To be specific, we use data of isothermal turbulence driven at two different spatial scales simultaneously. The driving wavenumbers are near $k \sim 2.5$ and $k \sim 20$. Since the two driving scales are well separated, we can assume that the large-scale driving (i.e., driving near $k \sim 2.5$) generates large-scale variations, while the small-scale driving (i.e., driving near $k \sim 20$) creates small-scale fluctuations. We want to remove the former and retain the latter. The sonic Mach number is around unity and the numerical resolution is 512^3 . The numerical setups for the simulation are virtually identical to those of the Run CS.L1.0.S2.0 in Yoo & Cho (2014), but the numerical resolution for the current run is higher. We list properties of turbulence in Table 1 (see Model L1.0.S2.0).

Since turbulence is driven at small and large scales simultaneously, it is not easy to define which are small-scale fluctuations and which are large-scale ones. Nevertheless, since our goal is to retrieve small-scale fluctuations, it is necessary to have rough estimates about the magnitudes of small-scale fluctuations. We calculate the standard deviations of the small-scale fluctuations, σ_Σ and σ_{V_c} , from the following procedure. First, we perform Fourier transformation of the real-space data and obtain wavevector-space data. Second, we filter out large-scale data. To be specific, we set the Fourier amplitudes to zero when $k < 10$ and retain the data when $k \geq 10$. We take $k = 10$ because the 3D spectra of velocity and density show different behaviors for $k < 10$ and $k > 10$ (see Section 3.2 for details). Third, we transform the filtered data back to real space. Fourth, we calculate σ_Σ and σ_{V_c} from the (filtered) real-space data. The resulting σ_Σ and σ_{V_c} are

$$\sigma_\Sigma \approx 16, \quad \text{and} \quad \sigma_{V_c} \approx 0.041, \quad (16)$$

which give

$$2(\sigma_\Sigma)^2 \approx 510, \quad \text{and} \quad 2(\sigma_{V_c})^2 \approx 0.033 \quad (17)$$

(see the data for KF2.5_20 in Table 1).

3. RESULTS

3.1. Sinusoidal large-scale variations

Figure 3 shows maps for column density (upper panels) and centroid velocity (lower panels). The far left panels (i.e., upper-left and lower-left panels) display maps without a large-scale variation. Since there is no large-scale variation, both column density and centroid velocity show only small-scale fluctuations. The panels in second, third, and last columns from the left display maps in the presence of large-scale variations with $\lambda = 2L, 2L/5$, and $2L/9$, respectively. As we can see in the maps, the large-scale variations of both column density and centroid velocity dominate small-scale ones.

Figure 4 shows our main results - the multi-point second-order structure functions. The order of the panels is the same as that of Figure 3. In case of small-scale fluctuations only (far left panels), all the structure functions are increasing functions of r when $r \lesssim 10$ and gradually approach the same constant value when $r > 10$, which is consistent with our expectation (see Figure 1(c)). The values of the structure functions for $r > 10$ are

$$SF_2(r > 10) \approx 1.5 \times 10^4 \quad (\text{for } \Sigma), \quad (18)$$

and

$$SF_2(r > 10) \sim 0.013 \quad (\text{for } V_c), \quad (19)$$

which are virtually identical to $2(\sigma_\Sigma)^2$ and $2(\sigma_{V_c})^2$, respectively (see Equation (14) and also Table 1).

In the presence of a large-scale variation with $\lambda=2L$ (i.e., $k = 1/2$; see Equation (15)), all structure functions, except SF_2^{2pt} (thin solid curves), can resolve the flat part ('plateau') quite well (see the panels in the second column from the left). The panels in the right two columns show that, when the wavelength λ of the large-scale variation becomes smaller, SF_2^{2pt} can no longer resolve the plateau. When $\lambda = 2L/5$ (the third panels from the left), SF_2^{4pt} and SF_2^{5pt} clearly resolve the plateau, while SF_2^{3pt} can barely resolve it. When $\lambda = 2L/9$ (far right panels), the multi-point structure functions marginally resolve the flat part. Among the multi-point structure functions shown in the panels, SF_2^{5pt} performs best. The values of the second-order structure functions at the plateau are very close to the values in Equation (14), or Equations (18) and (19), which means that we can indeed extract σ_Σ^2 or $\sigma_{V_c}^2$ using the multi-point structure functions.

3.2. Turbulent large-scale fluctuations

As explained in Section 2.2.2, we apply the multi-point structure functions to data of isothermal turbulence driven simultaneously at two different spatial scales. We plot the results in Figure 5: spectra of the 3D velocity and density (upper-left panel), spectra of the 2D column density and centroid velocity (upper-right panel), structure functions of column density (lower-left panel), and those of centroid velocity (lower-right panel).

The spectra of 3D velocity and density (upper-left panel) clearly show two peaks, one near the average wavenumber of large-scale driving ($k \sim 2.5$) and the other near the average wavenumber of small-scale driving ($k \sim 20$). The large-scale fluctuations of 3D velocity and density exhibit roughly power-law spectra for $k < 10$. Both spectra get flatter after $k \sim 10$ and the effects of

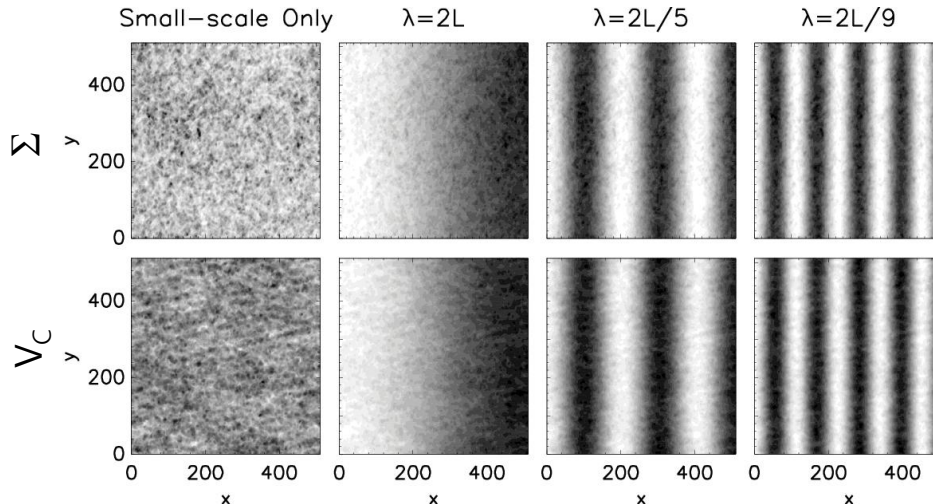


Figure 3. Contour plots of column density (upper panels) and centroid velocity (lower panels). The far left panels (i.e. panels in the first column from the left) show only small-scale fluctuations. Panels in the other columns contain both small-scale fluctuations, which are identical to the ones in the first column, and large-scale variations of sinusoidal forms (see Equation (15)). The large-scale variations dominate small-scale fluctuations. Note that λ denotes wavelength of the large-scale variations and $L = 2\pi$.

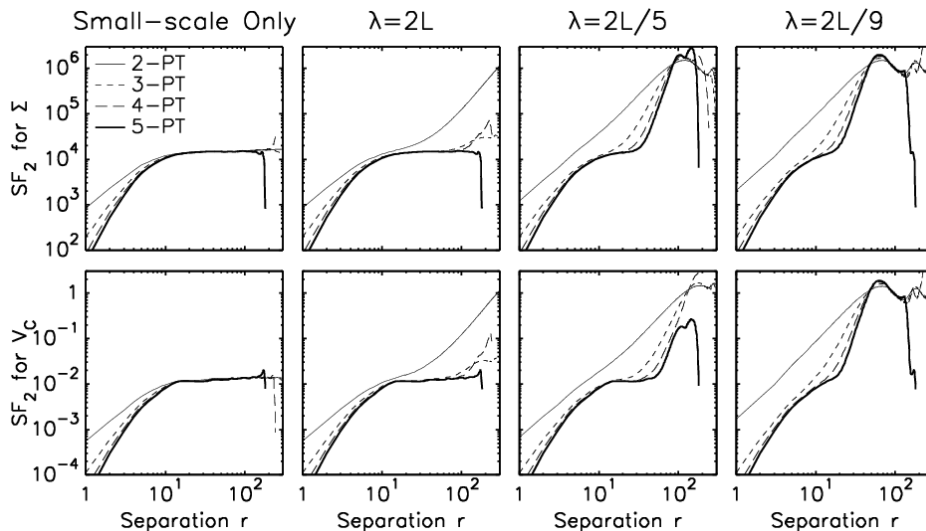


Figure 4. The multi-point second-order structure functions for column density (upper panels) and centroid velocity (lower panels). The arrangement of panels is the same as that of Figure 3. In the absence of large-scale variations (see the far left panels), all structure functions converge to a constant value for $r \gtrsim 10$. In the case of $\lambda = 2L$ (panels in the second column from the left), the two-point structure functions (thin solid lines) monotonically increase, while other multi-point structure functions have wide plateaus. In the case of $\lambda = 2L/5$ (panels in the third column from the left), the 3-point structure functions (dashed lines) also monotonically increase, which means that they cannot remove the large-scale variations well. In the case of $\lambda = 2L/9$ (far right panels), even the 5-point structure functions (thick solid lines) fail to resolve well-defined plateaus. Note that the 5-point structure function performs better than the other ones shown in the panels.

the small-scale driving become clearly visible for $k \gtrsim 15$. The behavior of the spectra of column density and centroid velocity (upper-right panel) is also similar. They decrease as the wavenumber increases for $k < 10$, become flat for $10 \lesssim k \lesssim 20$, and decrease again after $k \sim 20$. We may assume that the flat and decreasing spectra for $k \gtrsim 10$ are due to small-scale fluctuations.

The 2-point structure functions (SF_2^{2pt}) in the lower panels do not exhibit plateaus, while structure functions based on 3 or more points clearly show plateaus. The values of the multi-point second-order structure functions at

the plateaus are

$$SF_2(\text{at plateau}) \sim 800 \quad (\text{for } \Sigma) \quad (20)$$

and

$$SF_2(\text{at plateau}) \sim 0.005 \quad (\text{for } V_c), \quad (21)$$

which are not far from the estimates for $2(\sigma_\Sigma)^2$ and $2(\sigma_{V_c})^2$, respectively, in Equation (17). Therefore we can conclude that the multi-point structure functions can also remove complicated large-scale variations reasonably well.

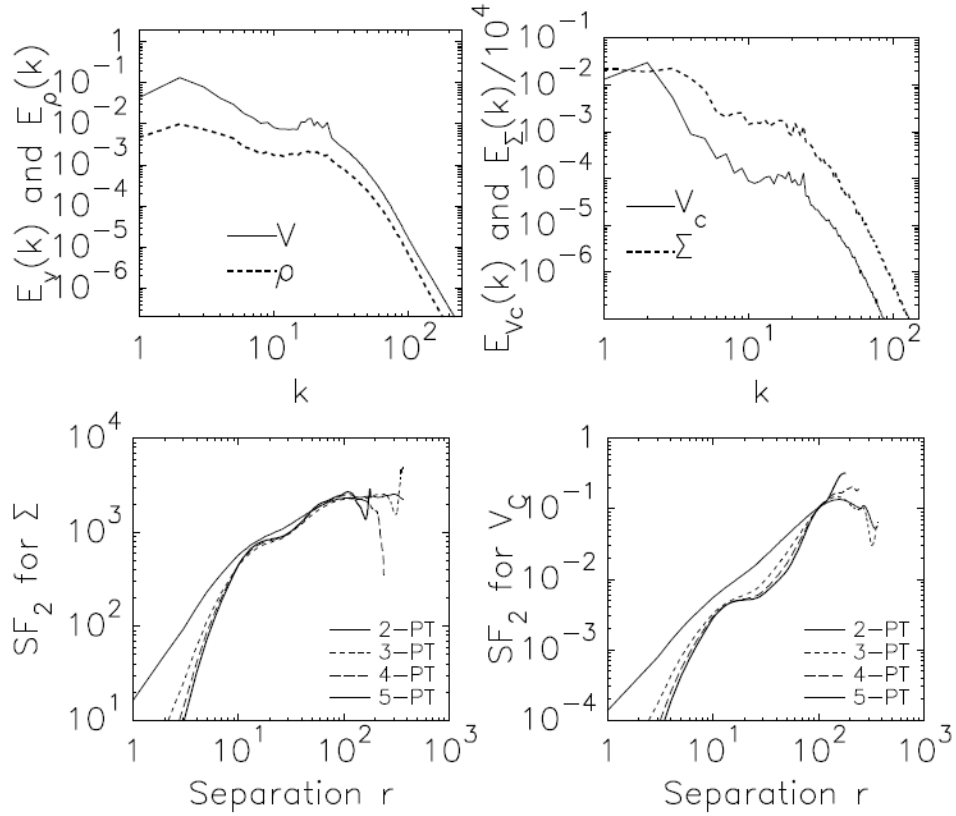


Figure 5. The Run K2.5_20. We drive the fluid at $k \sim 2.5$ and $k \sim 20$ simultaneously and generate transonic isothermal turbulence. We regard the structures generated by the large-scale driving (i.e., $k \sim 2.5$) as large-scale variations and the ones by the small-scale driving (i.e., $k \sim 20$) as small-scale fluctuations. *Upper-left:* Spectra of (3D) v and ρ . *Upper-right:* Spectra of (2D) column density Σ and centroid velocity V_c . *Lower-left:* Second-order structure functions for Σ . *Lower-right:* Second-order structure functions for V_c . Note the plateaus near $k \sim 15$.

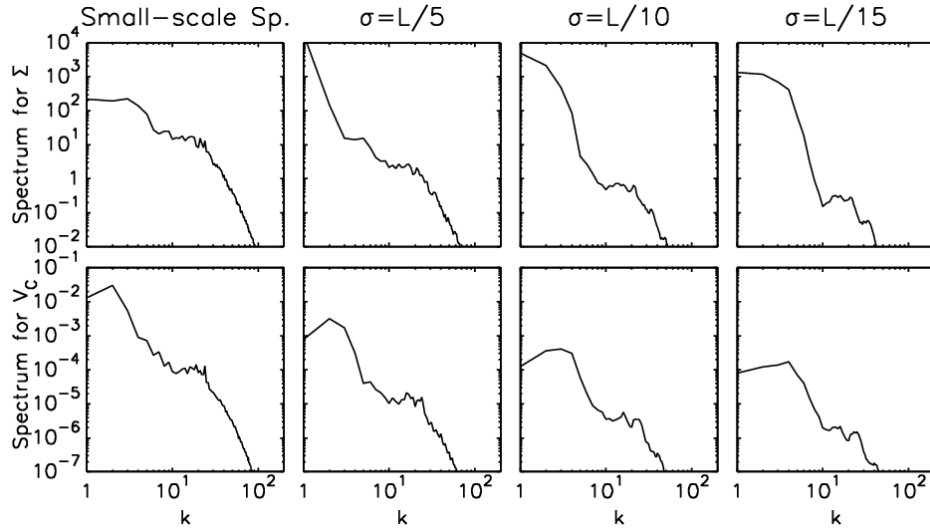


Figure 6. Spectra for column density (upper panels) and centroid velocity (lower panels). We use a data cube from the Run K2.5_20. We calculate spectra using either the original maps (512×512) or partial maps (256×256). The reason we use the partial maps is to include the edge effect. The plots in the first column from the left are the spectra of the original maps (on a grid of 512×512). The plots in the other columns are the spectra of the partial maps (on a grid of 256×256) tapered by gaussian windows with different widths (see the standard deviations σ 's of the window functions on the panels).

4.1. Spectrum vs. multi-point structure functions

Power spectrum is also a useful tool to study small-scale fluctuations. Indeed, if we can obtain the correct power spectrum, it may be possible to separate large-scale variations and small-scale fluctuations. However, obtaining the correct spectrum is not easy when the data are not periodic. If the data are not periodic, the discontinuity at the edge can severely affect the shape of the power spectrum. To reduce this artifact, a tapering window function is frequently used, which forces the values near the edge converge to zero. While the tapering method should work fine when there are only small-scale fluctuations, it may cause nontrivial effects when there are also large-scale variations.

To demonstrate the effects of tapering window, we calculate power spectra of non-periodic 2D maps using gaussian tapering windows. We make use of the column density and the centroid velocity maps of the Run K2.5_20, the resolution of which is 512×512 . In order to make the maps non-periodic we divide each map into 4 equal quadrants and take only one of them, the resolution of which is 256×256 . To be precise, the original periodic maps are define for $0 < x, y \leq 2\pi$ and the new non-periodic maps are defined for $0 < x, y \leq \pi$. We apply 2D gaussian tapering windows with different widths

$$W(x, y) = e^{[(x-\pi/2)^2 + (y-\pi/2)^2]/(2\sigma^2)}, \quad (22)$$

where $\sigma=L/5$, $L/10$, and $L/15$, to the non-periodic maps and calculate spectra. We plot the results in Figure 6. The upper and lower panels are for column density and centroid velocity, respectively. The far left panels show the spectra of the original maps (with 512×512 resolution), which should be identical to the spectra in the upper-right panel of Figure 5. Note that each spectra has two components - one for $k \lesssim 10$ and the other for $k \gtrsim 10$. The spectra in the other columns are the results of 2D gaussian tapering. From left to right, the standard deviation (σ) of the gaussian function decreases. In all the cases with the tapering windows, the small-scale component seems to be marginally visible. Nevertheless it may be difficult to draw any useful information from the spectra.

As we can see in Figure 6, the shape of spectrum changes when the shape of the tapering window changes. It may be possible to get a correct power spectrum if we know a proper shape of the window function *a priori*. The bottom line is that, although spectrum provides useful information on power distribution as a function of scale, it is not easy to obtain the correct spectrum. On the other hand, the multi-point structure functions do not require any knowledge *a priori*, which makes them more useful in deriving information on small-scale fluctuations.

4.2. Obtaining a small-scale map

Our technique discussed in earlier sections returns only the magnitudes of small-scale fluctuations. In this subsection, we demonstrate our technique can be also used to filter out large-scale variations and obtain a small-scale map. For simplicity, we use the 3-point (SF_2^{3pt}) and the 5-point (SF_2^{5pt}) second-order structure functions.

Suppose that we have a map of an observable quantity Q that contains both large-scale variations (Q_L) and small-scale fluctuations (Q_S). If SF_2^{3pt} or SF_2^{5pt} shows a plateau near a scale r_p , then we have

$$Q_L(\mathbf{x}) \approx [Q_L(\mathbf{x} + \mathbf{r}) + Q_L(\mathbf{x} - \mathbf{r})] / 2 \quad (23)$$

for SF_2^{3pt} and

$$Q_L(\mathbf{x}) \approx [4Q_L(\mathbf{x} + \mathbf{r}) + 4Q_L(\mathbf{x} - \mathbf{r}) - Q_L(\mathbf{x} + 2\mathbf{r}) - Q_L(\mathbf{x} - 2\mathbf{r})] / 6 \quad (24)$$

for SF_2^{5pt} (see the definitions of SF_2^{3pt} and SF_2^{5pt}), where \mathbf{x} is a point on the map, \mathbf{r} is a 2D displacement vector, and $|\mathbf{r}| \sim r_p$. Therefore, the 2-point average

$$\bar{Q}(\mathbf{x}) = \sum_{r_p - \Delta < |\mathbf{r}| < r_p + \Delta} [Q_L(\mathbf{x} + \mathbf{r}) + Q_L(\mathbf{x} - \mathbf{r})] / 2N \quad (25)$$

and the 4-point average

$$\bar{Q}(\mathbf{x}) = \sum_{r_p - \Delta < |\mathbf{r}| < r_p + \Delta} [4Q_L(\mathbf{x} + \mathbf{r}) + 4Q_L(\mathbf{x} - \mathbf{r}) - Q_L(\mathbf{x} + 2\mathbf{r}) - Q_L(\mathbf{x} - 2\mathbf{r})] / 6N \quad (26)$$

should be very good approximations for $Q_L(\mathbf{x})$. Here both $r_p - \Delta$ and $r_p + \Delta$ should lie in the plateau scale and N is the number of summation. Note that the multi-point averages are different from the usual (1-point) average with a top-hat window:

$$\bar{Q}(\mathbf{x}) = \sum_{|\mathbf{x} - \mathbf{x}'| < r_p} Q_L(\mathbf{x}') / N. \quad (27)$$

If we calculate a multi-point overage on a scale smaller than the plateau scale, the the value $\bar{Q}(\mathbf{x})$ contains part of small-scale fluctuations. On the other hand, if we calculate a multi-point overage on a scale larger than the plateau scale, then the value $\bar{Q}(\mathbf{x})$ loses some information about large-scale fluctuations.

After obtaining an approximate value of $Q_L(\mathbf{x})$ (i.e., $\bar{Q}(\mathbf{x})$), it is trivial to obtain the small-scale value $Q_S(\mathbf{x})$:

$$Q_S(\mathbf{x}) \approx Q(\mathbf{x}) - \bar{Q}(\mathbf{x}). \quad (28)$$

We may calculate spectrum of small-scale fluctuations using $Q_S(\mathbf{x})$.

In Figure 7 we demonstrate that this procedure is indeed working. We apply the multi-point average technique to the column density maps shown in Figure 3, in which we can clearly see that the large-scale variations dominate the small-scale fluctuations. We plot the results for the cases of $\lambda = 2L$ and $\lambda = 2L/5$ in Figure 7. We use $r_p = 17.5$ and $\Delta = 2.5$ (see Equations (25) and (26)). Note that, while both SF_2^{3pt} and SF_2^{5pt} for Σ have wide plateaus for $\lambda = 2L$, only SF_2^{5pt} has a reasonably wide plateau near $r = 17.5$ for $\lambda = 2L/5$ (see Figure 4). We plot the resulting small-scale maps of the usual 1-point average (Equation (27)), the 2-point average (Equation (25)), and the 4-point average (Equation (26)) in the first, the second, and the third column from the left, respectively. The upper panels are for $\lambda = 2L$ and the lower panels are for $\lambda = 2L/5$. As we can see in the contour plots, since the large-scale variation is

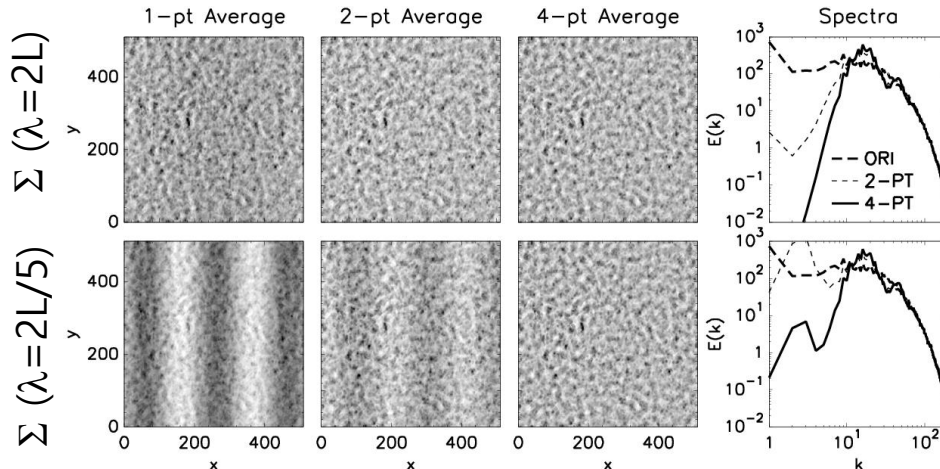


Figure 7. The reconstructed small-scale column density maps from the multi-point averaging technique for $\lambda = 2L$ (upper panels) and $2L/5$ (lower panels). We filter out the large-scale variations (see the maps in the second and third columns from the left in Figure 3) using the usual (1-point) average (Equation (27)), the 2-point average (Equations (25)), and the 4-point average (Equation (26)). The contour plots in the first, second, and third column from the left are maps reconstructed with the usual (1-point) averaging method, the 2-point averaging technique, and the 4-point averaging technique, respectively. The plots in the far right column show spectra. The thick long-dashed lines are for the original small-scale spectrum, which should be identical to the one in the upper-left panel of Figure 6. The dashed and the solid lines denote the spectra of the maps reconstructed with the 2-point and the 4-point average techniques, respectively. Note that all 3 spectra coincide well on small scales, which means that the multi-point average technique can be used to reconstruct small-scale maps and spectra.

smooth enough in the case of $\lambda = 2L$ (upper panels), all 3 averaging methods can remove the large-scale variation quite well. However, in the case of $\lambda = 2L/5$ (lower panels), the usual 1-point average and the 2-point average leave residuals of the large-scale variation on the maps, which means the usual 1-point average and the 2-point average cannot filter out the large-scale variation completely. The result of the usual 1-point average is worse than that of the 2-point average. On the other hand, filtering by the 4-point average does not leave visible residuals on the map (see the lower panel in the third column from the left). These results are not surprising because the 5-point structure function does have a well-defined plateau near $r \sim 17.5$, while the 3-point structure function doesn't.

The line plots in far right panels show the power spectra. The thick long-dashed lines in the upper and the lower panels denote the spectrum of the original small-scale map of column density (see the upper-left panel of Figure 3 for the original small-scale map). The dashed and the thick solid lines represent the spectra of the small-scale maps obtained by the 2-point and the 4-point average techniques, respectively. That is, they are spectra of the maps in the second and third columns in Figure 7. The spectra represented by the dashed and the thick solid lines do not have significant powers at small wavenumbers (i.e., $k \lesssim 10$). However, the spectrum represented by the dashed line in the lower panel clearly shows a peak near $k \sim 2.5$, which corresponds to the wavenumber of the large-scale variation. Note that the values of $E(k)$ is largest at $k = 2.5$ for the dashed line, which is in agreement with the fact that the residual of the large-scale variation is an outstanding feature of the map in second-lower panel from the left. The thick solid curve in the lower panel also has a peaks near $k \sim 2.5$. But, its value at $k = 2.5$ is not large, which is consistent with the fact that the residual of the large-scale variation

is not really visible on the map in the third-lower panel from the left. It is worth noting that the spectra from the 2-point and the 4-point average techniques virtually coincide with the spectrum of the original map when the wavenumber k is large.

4.3. Application to observations

In this paper, we have proposed and tested a technique to remove large-scale variations and obtain magnitudes of small-scale fluctuations. Our technique does not rely on fitting method that requires knowledge on a fitting function *a priori*. Although we have focused only on column density and centroid velocity in this paper, we can also apply our technique to FIR/sub-mm polarization, redshifted 21 cm observations, or synchrotron emission data. In principle, our technique is applicable to any data that contain large-scale and small-scale fluctuations, if their spatial/temporal/frequency scales are well separated. For example, we can use our technique to separate small-scale fluctuating velocity and large-scale rotational velocity. We can also use our technique to obtain variations of polarization angles in regions where magnetic fields have hourglass morphologies.

4.4. Construction of an n -point structure function

In general, we can construct an n -point second-order structure function as follows:

$$SF_2^{n-pt}(r) = \langle |\Delta^n|^2 \rangle \quad (29)$$

with

$$\Delta^n = \frac{1}{\mathcal{N}} \sum_{l=0}^{n-1} (-1)^l \binom{n-1}{l} Q \left(x + \left(\frac{n-1}{2} - l \right) r \right) \quad (30)$$

with

$$\mathcal{N} = \frac{1}{2} \sum_{l=0}^{n-1} \binom{n-1}{l}^2. \quad (31)$$

Table 1
Simulations.

Run	Resolution	M_s ^a	$B_0/\sqrt{4\pi\rho}$ ^b	k_f ^c	σ_{V_c} ^d	$2(\sigma_{V_c})^2$	σ_Σ ^e	$2(\sigma_\Sigma)^2$	A_Σ ^f	A_{V_c} ^g	HD or MHD
KF20	512 ³	~ 7	1	20	0.084	0.014	90	1.6×10^4	1024	1.0	MHD
KF2.5_20	512 ³	~ 1	0	2.5 & 20	0.041	0.0033	16	510	-	-	HD

^a The Sonic Mach number.^b The Alfvén speed of mean magnetic field.^c Central driving wavenumber.^d Standard deviation of centroid velocity of *small-scale* fluctuations. For KF2.5_20, we calculate σ_{V_c} using Fourier velocity and density modes with $k \geq 10$ (see text for details).^e Standard deviation of column density of *small-scale* fluctuations. For KF2.5_20, we calculate σ_Σ using Fourier density modes with $k \geq 10$ (see text for details).^f Amplitude of large-scale column density. See Equation (15).^g Amplitude of large-scale centroid velocity. See Equation (15).

Here $\binom{n}{l}$ is the binomial coefficient and $(n-1)/2$ can be either $n/2$ or $n/2 - 1$ if n is an even number. Note that Δ^n is the same as the n -th order central difference.

4.5. Summary

In summary, we have obtained the following results.

1. We develop a technique that can remove large-scale variations in observable quantities. Our technique relies on multi-point structure functions and gives us magnitudes of small-scale fluctuations (see Equations (7)-(9), and (29)).
2. Our technique works fine for a large-scale variation of a simple sinusoidal form. It also works reasonably well for a more complicated turbulent large-scale fluctuations.
3. If a second-order structure function shows a plateau, then the variance of the small-scale fluctuations is equal to the value of the structure function at the plateau divided by two (Equation (10)).
4. Our technique can be used to separate small-scale fluctuations and large-scale variations. We have discussed how to filter out large-scale variations and obtain maps of small-scale fluctuations using multi-point averages (Section 4.2).

This work is supported by the National R & D Program through the National Research Foundation of Korea Grants funded by the Korean Government (NRF-2016R1A5A1013277 and NRF-2016R1D1A1B02015014). We thank Hyunju Yoo for providing the data cube of the Run KF2.5_20. We also thank Min-Young Lee for useful discussions.

REFERENCES

Burkhart, B., Falceta-Gonçalves, D., Kowal, G., & Lazarian, A. 2009, ApJ, 693, 250
 Chandrasekhar, S., & Fermi, E. 1953, ApJ, 118, 113

Cho, J. 2017, Journal of Physics Conference Series, 837, 012002
 Cho, J., & Lazarian, A. 2009, ApJ, 701, 236
 Cho, J., Lazarian, A., & Timbie, P. T. 2012, ApJ, 749, 164
 Cho, J., & Yoo, H. 2016, ApJ, 821, 21
 Crutcher, R. M., Nutter, D. J., Ward-Thompson, D., & Kirk, J. M. 2004, ApJ, 600, 279
 Curran, R. L., & Chrysostomou, A. 2007, MNRAS, 382, 699
 Di Francesco, J., Myers, P. C., Wilner, D. J., Ohashi, N., & Mardones, D. 2001, ApJ, 562, 770
 Dickman, R. L., & Kleiner, S. C. 1985, ApJ, 295, 479
 Esquivel, A., Lazarian, A., Horibe, S., et al. 2007, MNRAS, 381, 1733
 Falcon, E., Fauve, S., & Laroche, C. 2007, Physical Review Letters, 98, 154501
 Girart, J. M., Rao, R., & Marrone, D. P. 2006, Science, 313, 812
 Gonatas, D. P., Engargiola, G. A., Hildebrand, R. H., et al. 1990, ApJ, 357, 132
 González-Casanova, D. F., & Lazarian, A. 2017, ApJ, 835, 41
 Heyer, M., Gong, H., Ostriker, E., & Brunt, C. 2008, ApJ, 680, 420
 Hildebrand, R. H., Kirby, L., Dotson, J. L., Houde, M., & Vaillancourt, J. E. 2009, ApJ, 696, 567
 Houde, M., Dowell, C. D., Hildebrand, R. H., et al. 2004, ApJ, 604, 717
 Houde, M., Vaillancourt, J. E., Hildebrand, R. H., Chitsazzadeh, S., & Kirby, L. 2009, ApJ, 706, 1504
 Imara, N., & Blitz, L. 2011, ApJ, 732, 78
 Kleiner, S. C., & Dickman, R. L. 1985, ApJ, 295, 466
 Lazarian, A., & Pogosyan, D. 2008, ApJ, 686, 350-362
 Lai, S.-P., Crutcher, R. M., Girart, J. M., & Rao, R. 2001, ApJ, 561, 864
 Mao, S. A., Gaensler, B. M., Stanimirović, S., et al. 2008, ApJ, 688, 1029
 Miesch, M. S., & Bally, J. 1994, ApJ, 429, 645
 Monin, A. S., & Iaglom, A. M. 1975, Statistical Fluid Mechanics (Cambridge, Mass.: MIT Press)
 Morales, M. F., Bowman, J. D., & Hewitt, J. N. 2006, ApJ, 648, 767
 O'dell, C. R., & Castaneda, H. O. 1987, ApJ, 317, 686
 Pattle, K., Ward-Thompson, D., Berry, D., et al. 2017, arXiv:1707.05269
 Schleuning, D. A. 1998, ApJ, 493, 811
 Sugitani, K., Nakamura, F., Tamura, M., et al. 2010, ApJ, 716, 299
 Sugitani, K., Nakamura, F., Watanabe, M., et al. 2011, ApJ, 734, 63
 Tang, Y.-W., Ho, P. T. P., Girart, J. M., et al. 2009, ApJ, 695, 1399
 von Hoerner, S. 1951, Zeitschrift für Astrophysik, 30, 17
 Yoo, H., & Cho, J. 2014, ApJ, 780, 99